ACS Catalysis

Research Article

Cite This: ACS Catal. 2017, 7, 7610-7622

pubs.acs.org/acscatalysis

Spinel-Structured $ZnCr_2O_4$ with Excess Zn Is the Active ZnO/Cr_2O_3 Catalyst for High-Temperature Methanol Synthesis

Huiqing Song,[†] Daniel Laudenschleger,[†] John J. Carey,[‡] Holger Ruland,[†] Michael Nolan,*[,‡] and Martin Muhler*[,†]

[†]Laboratory of Industrial Chemistry, Ruhr-University Bochum, 44780 Bochum, North Rhine-Westphalia, Germany

[‡]Tyndall National Institute, University College Cork, Cork T12R5CP, Munster, Ireland

Supporting Information

ABSTRACT: A series of ZnO/Cr_2O_3 catalysts with different Zn:Cr ratios was prepared by coprecipitation at a constant pH of 7 and applied in methanol synthesis at 260−300 °C and 60 bar. The X-ray diffraction (XRD) results showed that the calcined catalysts with ratios from 65:35 to 55:45 consist of $ZnCr_2O_4$ spinel with a low degree of crystallinity. For catalysts with Zn:Cr ratios smaller than 1, the formation of chromates was observed in agreement with temperature-programmed reduction results. Raman and XRD results did not provide evidence for the presence of segregated ZnO, indicating the existence of Zn-rich nonstoichiometric Zn−Cr spinel in the calcined catalyst. The catalyst with Zn:Cr = 65:35 exhibits the best performance in methanol synthesis. The Zn:Cr ratio of this catalyst corresponds to that of the $Zn_4Cr_2(OH)_{12}CO_3$ precursor with hydrotalcite-like structure obtained by coprecipitation, which is converted during calcination into a nonstoichiometric Zn−Cr spinel with an optimum amount of oxygen vacancies resulting in high activity in methanol synthesis. Density functional theory calculations are used to examine the formation of oxygen vacancies and to measure the reducibility of the methanol synthesis catalysts. Doping Cr into bulk and the (10−10) surface of ZnO does not enhance the reducibility of ZnO, confirming that Cr:ZnO cannot be the active phase. The (100) surface of the $ZnCr_2O_4$ spinel has a favorable oxygen vacancy formation energy of 1.58 eV. Doping this surface with excess Zn charge-balanced by oxygen vacancies to give a 60% Zn content yields a catalyst composed of an amorphous ZnO layer supported on the spinel with high reducibility, confirming this as the active phase for the methanol synthesis catalyst.

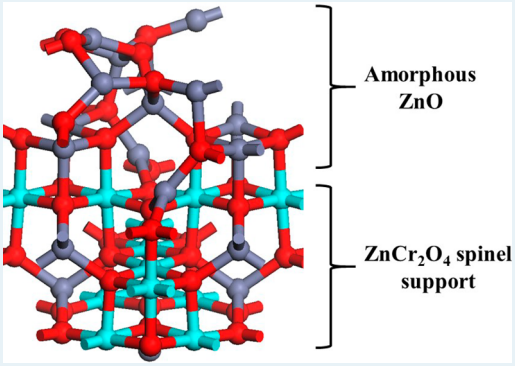

KEYWORDS: *ZnO/Cr_2O_3, methanol synthesis, nonstoichiometric spinel, oxygen vacancy, DFT+U*

1. INTRODUCTION

Methanol is one of the most important industrially produced basic chemicals because of its application in a wide range of fields.[1,2] The investigation of methanol synthesis from a mixture of hydrogen and carbon oxides using metals and metal oxides as catalyst dates back to the 1910s.[3] In the 1920s, BASF issued two patents focusing on ZnO/Cr_2O_3 and Cu/ZnO catalysts, which were primarily used in the early period of the industrial production of methanol.[4,5] Later, the $Cu/ZnO/Al_2O_3$ catalyst with high activity and selectivity was patented by ICI in the 1960s, which requires highly purified synthesis gas.[6,7] Because of its lower operating temperature and pressure, the Cu/ZnO-based catalyst has been used extensively for methanol production in the last decades. However, Zn−Cr mixed oxides, which are applied in the synthesis of methanol at high temperatures and pressures,[8] remain of interest owing to their resistance against sulfur impurities in syngas as well as the possibility of modifying their selectivities toward the synthesis of higher alcohols.[9−12] Furthermore, because of their high thermal stability, ZnO/Cr_2O_3 catalysts demonstrated great potential in combination with microporous acidic catalysts in the one-pot synthesis of liquid hydrocarbons and short chain olefins from syngas.[13,14]

In the early investigation on methanol synthesis over ZnO/Cr_2O_3 catalysts prepared by coprecipitation followed by calcination, the synergy observed between ZnO and Cr_2O_3 in comparison to the pure component oxides was mainly ascribed to an increase in the specific surface area.[15] In addition, ZnO had been generally identified as the only active component, and the promoting role of Cr_2O_3 was attributed to spinel formation, which prevented the sintering of small ZnO crystallites by providing a considerably larger surface area and better distribution of ZnO particles.[8] It is generally accepted that methanol synthesis over ZnO is a structure-sensitive reaction, in which oxygen vacancies on ZnO (000-1) are assumed to be the active sites. One model, which was reported by Boccuzzi et al.[16] in 1978, described an active site composed of three Zn ions around an oxygen vacancy. Two years later, an active site with

Received: June 4, 2017
Revised: September 25, 2017
Published: September 27, 2017

DOI: 10.1021/acscatal.7b01822
ACS Catal. 2017, 7, 7610−7622

similar geometry and composition was proposed by Kung,[17] who assumed that oxygen vacancies could assist in the adsorption and activation of CO. He proposed a catalytic cycle of methanol formation based on the oxygen vacancy as active site. The reaction starts with the dissociative adsorption of H_2 on ZnO sites around the oxygen vacancy followed by the adsorption of the CO molecule in the oxygen vacancy. The reaction proceeds through hydrogenation of adsorbed CO by the transfer of adsorbed hydrogen to form surface formyl species $(CHO)_{ads}$. Further hydrogenation of the formyl species yields adsorbed formaldehyde $(H_2CO)_{ads}$, which is hydrogenated forming methoxy species $(H_3CO)_{ads}$. The hydrogenation of methoxy species leads to the product methanol. It was proposed that a change of the mechanism occurs when CO_2 is present, as the very stable formate $(HCO_2)_{ads}$ species may be formed in the defect site. This mechanism was confirmed by Kurtz et al.,[18] who found that in the presence of CO_2 the rate of methanol formation is significantly slower.

In addition to ZnO, nonstoichiometric Zn−Cr spinel was reported as the active phase in methanol synthesis. Del Piero et al.[19] first reported that the nonstoichiometric Zn−Cr spinel was formed by the dissolution of excess ZnO in $ZnCr_2O_4$, which results from the solid reaction between ZnO and Cr_2O_3 during calcination. They also pointed out that the dissolved Zn^{2+} ions may be located in octahedral sites randomly substituting Cr^{3+} ions, leaving some of the tetrahedral sites vacant. The deactivation of the catalyst was observed to be accompanied by a decrease in the nonstoichiometry of the spinel-like phase and a corresponding increase in the amount of crystalline ZnO detected by X-ray diffraction (XRD). Therefore, they assumed the nonstoichiometric spinel-like phase to be the active phase in the ZnO/Cr_2O_3 catalyst. More studies regarding the influence of the nonstoichiometry of the Zn−Cr spinel on its bulk and surface properties were carried out by Bertoldi et al.,[20] who proposed a general chemical formula of the nonstoichiometric Zn−Cr spinel as $Zn_xCr_{2/3(1-x)}O$, where x ranges from 0.25 to 0.40. They also found that the activity of the nonstoichiometric Zn−Cr spinel toward CO adsorption is much higher than observed for pure ZnO, Cr_2O_3, and $ZnCr_2O_4$. Giamello et al.[21] and Riva et al.[22] also confirmed the formation of the nonstoichiometric Zn−Cr spinel based on methanol temperature-programmed desorption (TPD) and X-ray photoelectron spectroscopy (XPS) studies. Grimes et al.[23] used atomistic simulation to explain the mechanisms of the dissolution of ZnO and suggested that one oxygen vacancy was created for every three ZnO species dissolved.

The Zn:Cr ratio was found to significantly influence the catalytic activity of the ZnO/Cr_2O_3 catalyst.[24] The optimum Zn:Cr ratio has been extensively investigated in the literature.[8,25,26] Molstad and Dodge[25] reported that catalysts with Zn:Cr ratios between 70:30 and 60:40 exhibit the highest yield of methanol at relatively low temperatures of 300−325 °C. This observation is in good agreement with the results reported by Bone,[24] who found that the maximum activity is achieved with a Zn-excess catalyst containing about 75 atom % of Zn. According to Molstad and Dodge,[25] the highest activity was obtained with the catalyst containing 20−30 atom % of Cr at a reaction temperature in the range from 350 to 425 °C. Additionally, they observed that the catalysts with Zn:Cr > 75:25 lose their activity rapidly, while the catalysts containing more Cr exhibit a slight activity increase with reaction time. Furthermore, after testing, the catalysts had undergone volume shrinkage, which increased with increasing Cr content. When using the already shrunk catalyst, the maximum yield of methanol was obtained with a Zn:Cr ratio of around 1:1. These results were also confirmed by Errani et al.,[26] however, with a different explanation. Based on the investigation of nonstoichiometric Zn−Cr spinel,[19−22] the authors suggested that the activity increases up to Zn:Cr = 50:50 due to the increasing nonstoichiometry of the spinel-type phase, while the formation of a segregated ZnO phase causes a decrease in activity. Nevertheless, no linear correlation was found between the catalytic activity and the excess zinc inside the nonstoichiometric spinel-type structure up to Zn:Cr = 50:50. More recently, Bradford et al.[27] reported that ZnO/Cr_2O_3 catalysts prepared by coprecipitation exhibited a maximum specific activity for Zn:Cr = 2.56 (72:28), which is in good agreement with Molstad and Dodge.[25] Although the influence of the Zn:Cr ratio on the performance of ZnO/Cr_2O_3 catalyst has been investigated over decades, there is still no agreement on the optimal Zn:Cr ratio.

In this work, we studied the role of the Zn:Cr ratio in the catalytic activity of ZnO/Cr_2O_3 catalysts by a combined experimental and density functional theory (DFT) approach. A series of ZnO/Cr_2O_3 catalysts with different Zn:Cr ratios varying from 100:0 to 0:100 were prepared by coprecipitation at 65 °C and pH 7 with Na_2CO_3 solution as the precipitating agent. The resulting precipitates were calcined in air at 320 °C for 3 h and characterized by N_2 physisorption, XRD, temperature-programmed reduction (TPR), XPS, and Raman spectroscopy. The catalytic testing was performed at 60 bar using a syngas mixture with H_2:CO = 1.5, and the reaction temperature was varied in steps of 20 °C from 260 to 300 °C. The catalyst with Zn:Cr = 65:35 exhibits the best performance in methanol synthesis.

Given that previous work shows the importance of oxygen vacancies in methanol synthesis, we combine these experiments with DFT calculations of the reducibility of different Cr/Zn-containing systems, as measured by the oxygen vacancy formation energy. For a catalyst composed of Cr doping into ZnO (as excess Zn), the oxygen vacancy formation energies are larger than undoped ZnO. The oxygen vacancy formation energies for the pure $ZnCr_2O_4$ spinel are significantly lower than the undoped ZnO. Doping the spinel structure with excess Zn on Cr^{3+} octahedral sites gives compositions ranging from 30% to 60% Zn content. At the higher concentration of incorporated Zn, the Zn dopants replace all surface Cr atoms (it is less favorable to replace bulk Cr atoms), and the oxygen vacancy formation energy decreases, indicating high reducibility of this system. The structure of this catalyst can be thought of as a thin, amorphous ZnO-stoichiometry layer supported on the $ZnCr_2O_4$ spinel. In addition, the adsorption of CO and H_2 on $ZnCr_2O_4$ with excess Zn is weaker than on stoichiometric $ZnCr_2O_4$, allowing for increased reactivity. These DFT insights help to explain the experimental observations that both ZnO and $ZnCr_2O_4$ are present in the catalyst. The reducibility of and interaction with CO and H_2 on $ZnCr_2O_4$ are the key to increased methanol activity and a superior methanol synthesis catalyst.

2. EXPERIMENTAL SECTION

Catalyst Preparation. Catalysts with different Zn:Cr ratios were prepared by a coprecipitation procedure adapted from Kurtz et al.[18] A metal salt solution (1 M) consisting of zinc and chromium nitrates with the desired Zn:Cr ratio was added dropwise into a vessel, which contained 50 mL of HPLC water

DOI: 10.1021/acscatal.7b01822
ACS Catal. 2017, 7, 7610−7622

heated up to 65 °C.The precipitation was performed under continuously stirring at a constant pH of 7 by simultaneous addition of Na_2CO_3 solution (1.2 M) using an autotitrator while the precipitation temperature was constantly kept at 65 °C. The suspension after precipitation was aged at 65 °C for 2 h. Subsequently, the precipitate was filtered and washed with HPLC water and then dried for 18 h at 120 °C. The dried precipitate was granulated and calcined in synthetic air for 3 h with a heating rate of 2 °C min^{-1} to 320 °C and keeping this temperature for 3 h.

Characterization. The metal composition as well as the content of residual Na were determined by optical emission spectroscopy with inductively coupled plasma (ICP-OES) using an UNICAM PU 7000. Powder XRD was performed using a Panalytical MPD diffractometer with Cu Kα radiation (λ = 0.154 nm) at 45 kV and 40 mA without monochromator. A Ni filter was used to suppress the Kß emission line.The XRD patterns were recorded over a 2θ range of 5−85° with a 0.0131 step width and 250 s collection time. Powder diffraction files (PDF) from the International Center of Diffraction Data (ICDD) and X'PertHighScore Plus software were applied for qualitative phase analysis. Specific surface areas and pore structures were measured by N_2 physisorption at 77 K using a Quantachrome Autosorb-1-MP instrument. The catalysts were degassed under vacuum at 200 °C for 2 h prior to the measurement. Pore volume and average pore diameter were obtained using the Barrett−Joyner−Halenda (BJH) method. TPR was carried out in a U-tube quartz reactor with a H_2/Ar mixture containing 4.6% H_2 as reducing agent. About 100 mg of catalysts (250−355 μm sieve fraction) was flushed with Ar (99.9995%) to remove weakly bound water and then reduced using a total flow rate of 84.1 N mL/min at a rate of 5 °C/min with a programmable temperature controller. The samples were heated up to 800 °C, and temperature was held at 800 °C for 1 h. H_2 consumption was recorded by a thermal conductivity detector (TCD). The effluent gas passed through a cold trap filled with isopropanol and dry ice before entering the TCD in order to remove water formed during reduction. XPS measurements were carried out in an ultrahigh vacuum setup equipped with a high-resolution Gammadata-Scienta SES 2002 analyzer and a monochromatic Al Kα as the X-ray source (1486.6 eV, anode operating at 14 kV and 30 mA). The base pressure in the measurement chamber was maintained at about 7×10^{-10} mbar. The measurements were performed in the fixed transmission mode with a pass energy of 200 eV. Charging effects during the measurements were compensated by applying a flood gun. The measured spectra were calibrated on the basis of the C 1s peak at 284.5 eV originating from adsorbed hydrocarbons. The CasaXPS software was used to analyze the XPS data.

Raman spectra were measured using a WITec confocal Raman microscope Alpha300 R/S/A. The samples excitation was carried out by using a 532 nm frequency-doubled Nd:YAG laser. A 50×/0.4 NA objective was used to focus the laser onto the sample. The backscattered Raman light was collected by the same objective and transferred via a 50 μm multimode fiber to the spectrometer unit consisting of a 600 lines/mm diffraction grating and a 1600 × 200 pixels electron multiplying charge-coupled device camera operating at 60 °C. The spectral resolution was approximately 4 cm^{-1}. Ten Raman spectra of each sample were recorded with an integration time of 30 s for each spectrum at a laser power of 20 mW.

Continuous Methanol Synthesis Setup. The setup for methanol synthesis from syngas (Figure S1) consists of the gas supply unit, the reactor unit, and the gas chromatograph as analytical device. The gas supply includes syngas, Ar, H_2, and H_2 diluted in He. In the present work, syngas with a ratio of H_2:CO = 1.5 containing 10% N_2 as internal standard was used for the catalytic tests.

In the reactor unit, the main gas line was split into 4 branch lines connected to 4 separate reactors. Each branch line consisted of a MFC, a valve, a back-pressure valve, and two filters. All 4 reactors were mounted in an oven, which established the reaction temperature in the range from 260 to 300 °C. The desired pressure for the reaction was controlled by a pressure regulator with proportional-integral-differential (PID) controllers. The outlet gas of the chosen reactor was introduced into the GC by switching the multiposition valve (VM), while the gas mixtures from the other reactors were passed to the exhaust. In order to avoid product condensation in the gas mixture, all gas lines from the reactor outlet to the GC were installed in a separate oven, in which the temperature was set to 155 °C. The reactors were made of stainless steel and coated with glass on the inner wall. The catalyst was fixed between two plugs of quartz wool in the middle of the reactor, and two glass rods were placed in the reactors to reduce the dead volume.

Catalytic Tests. Catalyst (500 mg) with particle sizes of 250−355 μm was loaded in each glass-lined stainless steel reactor. No prereduction was carried out prior to the catalytic tests. Methanol synthesis was performed at 60 bar using a mixture of 36% CO, 54% H_2, and 10% N_2 at a volumetric feed rate of 40 mL min^{-1} (STP) resulting in a GHSV of 4800 mL h^{-1} g_{cat}^{-1}. The reaction temperature was varied in steps of 20 °C from 260 to 300 °C. At each temperature, the reaction was carried out for 20 h. Online gas analysis was performed with an Agilent gas chromatograph equipped with two thermal conductivity detectors using He as carrier gas.

Computational Methodology. All calculations are carried out using density functional theory (DFT) with the generalized gradient approximation (GGA)[28] and the Perdew−Burke−Ernzerhof (PBE)[29] exchange correlation functional as implemented in the Vienna ab initio Simulation Package (VASP).[30,31] The valence electrons are expanded using a plane wave basis set, and the interactions between the core (Cr:[Ar], Zn:[Ar], O:[He]) and the valence electrons (Cr:[$3p^6$, $3d^5$, $4s^1$], Zn:[$3d^{10}$, $4s^2$], O:[$2s^2$, $2p^4$]) are treated using the projected augmented wave (PAW) method.[32] To describe the strong electron correlation of Cr cations in Cr-ZnO and in the spinel structure, a Hubbard + U correction (giving DFT +U)[33,34] is applied to the Cr 3d states, for which the value of U is 5 eV.[35,36] Due to doping of lower valent Zn^{2+} cations onto Cr^{3+} sites, oxygen hole states will form and in describing these states we apply U = 5.5 eV[36] to the O 2p states.

The low-energy structures for the ZnO bulk and $ZnCr_2O_4$ spinel bulk are obtained by relaxing a series of structures from −4% to +4% of the experiment lattice constant where the atomic positions, cell vectors, and angles were allowed to relax at a constant volume. The energies obtained from each structure were fitted to the Murnaghan Equation of State[37] to obtain the minimum-energy structure. This was carried out for different plane wave cutoff energies of 400, 450, and 500 eV where the Brillouin Zone integrations were sampled using the Monkhorst−Pack method[38] at different k-point sampling grids of 2 × 2 × 2, 4 × 4 × 4, and 6 × 6 × 6. The structures were

DOI: 10.1021/acscatal.7b01822
ACS Catal. 2017, 7, 7610−7622

Table 1. Nominal and Actual Metal Composition As Well As the Textural Properties of the Catalysts after Calcination

catalyst	nominal Zn:Cr ratio (atomic)	actual Zn:Cr ratio (atomic)	Na (wt %)	A_{BET} (m^2 g^{-1})	r_p (nm)	V_p (cm^3 g^{-1})
100Zn	100:0	100:0	0.1	34	6.8	0.14
80Zn20Cr	80:20	83:17	0.2	82	2.4	0.11
70Zn30Cr	70:30	71:29	0.03	95	2.9	0.18
65Zn35Cr	65:35	67:33	0.04	106	2.7	0.18
60Zn40Cr	60:40	62:38	0.01	117	1.8	0.17
55Zn45Cr	55:45	57:43	0.3	112	2.4	0.18
50Zn50Cr	50:50	51:49	0.7	85	1.9	0.12
40Zn60Cr	40:60	46:54	2.8	34	1.9	0.07
33Zn66Cr	33:66	35:65	4.1	18	1.9	0.05
20Zn80Cr	20:80	28:72	7.2	2	2.4	0.00
100Cr	0:100	0:100	8.1	3	9.2	0.03

deemed converged when the forces on the atoms were less than 0.02 eV/Å. For both bulk structures, the parameters for the bulk structure are a plane wave cutoff energy of 450 eV and a k-point sampling grid of 4 × 4 × 4, which gives a deviation of 1.6% from the experimental lattice constants for both bulk structures.[39,40]

The ZnO bulk structure was expanded to a 3 × 3 × 3 supercell ($Zn_{54}O_{54}$) and relaxed using a reduced Gamma centered k-point sampling grid of 1 × 1 × 1 with the same energy cutoff, while the $ZnCr_2O_4$ spinel bulk was expanded to a 1 × 1 × 2 supercell structure ($Zn_{16}Cr_{32}O_{64}$) with a reduced k-point sampling grid of 4 × 4 × 2. The bulk structures were expanded to accommodate point defects under periodic boundary conditions for investigations of Cr doping and oxygen vacancy formation in each of the systems of interest.

The nonpolar ZnO (10−10) and $ZnCr_2O_4$ (100) surfaces are also examined as model catalysts to explore different possible structures and compositions, with Cr:Zn ratios ranging from 0−100%. The surfaces are generated from the lowest-energy bulk structures and modeled using the slab method. For ZnO (10−10) and $ZnCr_2O_4$ (100), slab thicknesses of 13 and 10 Å, with 9 and 11 atomic layers, are used. The vacuum region above the surface is 13 Å. The bottom 3 layers of each slab are fixed while the rest of the slab is allowed to fully relax. The surfaces are converged using the same parameters as the bulk calculations

The different compositions of the Cr:ZnO systems in the experimental catalysts are modeled by Cr^{3+} doping in ZnO and Zn^{2+} doping on a Cr site in $ZnCr_2O_4$ spinel using the bulk and surface structures. A key property identified experimentally for methanol synthesis catalyst is the reducibility, which is modeled by oxygen vacancy formation. We investigate the effect of doping on the reducibility. The doping of these structures is carried out in a similar manner to previous studies for charge compensating mechanisms for doping in Cr_2O_3,[36] CeO_2,[41−43] or TiO_2[44] by first examining any charge compensating oxygen vacancies in the doped system and then calculating the formation energy of the next oxygen vacancy, which reduces the oxide. We also investigate the interaction with CO and H_2 by adsorbing the molecules on different sites of the stoichiometric $ZnCr_2O_4$ and Zn-rich $ZnCr_2O_4$ (100) surfaces, computing the adsorption energy of each molecule as follows:

$$E^{ads} = E(CO/H_2{-}ZnCr_2O_4) - [E(CO/H_2) + E(ZnCr_2O_4)]$$

where $E(CO/H_2{-}ZnCr_2O_4)$ is the total energy of CO or H_2 adsorbed at the spinel (100) surface, $E(CO/H_2)$ is the total energy of the free molecule, and $E(ZnCr_2O_4)$ is the total energy of the spinel (100) surface.

The changes in oxidation states of the cations in the bulk structures was investigated using Bader's atoms in molecules method as implemented in VASP by Henkelman et al.[45−47] and spin magnetization values.

3. RESULTS

Characterization of the Catalyst Precursors. The actual metal compositions of the calcined precursors determined by ICP-OES as well as the textural properties determined by N_2 physisorption are summarized in Table 1. Small variations between the nominal and actual Zn:Cr ratio can be observed for all the catalysts. More specifically, the actual amount of Cr in the catalysts is always less than expected. Based on the calculation of the maximal concentration of ionic Cr after precipitation, the possibility of incomplete precipitation of Cr^{3+} can be excluded. Hence, the loss of Cr probably occurred during the filtration. The Cr-containing precipitates formed with a very small particle size during the coprecipitation were most likely $Cr(OH)_3$ nanoparticles,[48] and a part of these precipitates penetrated the glass fiber filter during the filtration. For the catalysts containing high amounts of Cr, a considerably high amount of Na residue was found to be present. This difficulty of removing Na may be also caused by the small-sized $Cr(OH)_3$ nanoparticles formed by coprecipitation. The reaction between acidic $Cr(OH)_3$ and the basic Na residue presumably prevents the complete removal of Na.[49] For the catalysts with lower Zn:Cr ratio, more small-sized $Cr(OH)_3$ was formed, resulting in more difficult filtration and washing.

The specific surface area strongly depends on the Zn:Cr ratio of the catalysts. With decreasing nominal Zn:Cr ratio from 100:0 to 60:40 the specific surface area increases, and for Zn:Cr= 60:40, the specific surface area reaches a maximum of 117 m^2 g^{-1}. A further decrease of the nominal Zn:Cr ratio from 60:40 to 0:100 results in a decrease in specific surface area.

When the composition of the catalyst is changed from excess of Zn to excess of Cr, the specific surface area undergoes a drastic decline. In this work, the catalysts containing high levels of Cr generally exhibit lower surface areas and smaller pore volumes compared with the catalysts containing high amounts of Zn due to the high contents of Na residue. This trend in the specific surface area of the catalysts scales with the catalytic activity shown in section b. Catalytic tests, indicating that surface area is a major factor that influences the catalytic activity of the ZnO/Cr_2O_3 catalysts. It should also be noted that both pure ZnO and Cr_2O_3 exhibit a significantly smaller surface area than the ZnO/Cr_2O_3 catalysts with high Zn:Cr ratio between

DOI: 10.1021/acscatal.7b01822
ACS Catal. 2017, 7, 7610−7622

80:20 and 50:50. Therefore, in the ZnO/Cr_2O_3 catalyst system, Cr_2O_3 probably does not act as a traditional support material that directly increases the surface of the catalyst. Instead, $ZnCr_2O_4$ is the actual support that increases the surface area of the catalyst and improves the distribution of ZnO.[8]

The XRD patterns of the hydroxycarbonate precursors before calcination are shown in Figure 1. For 100Zn, most of

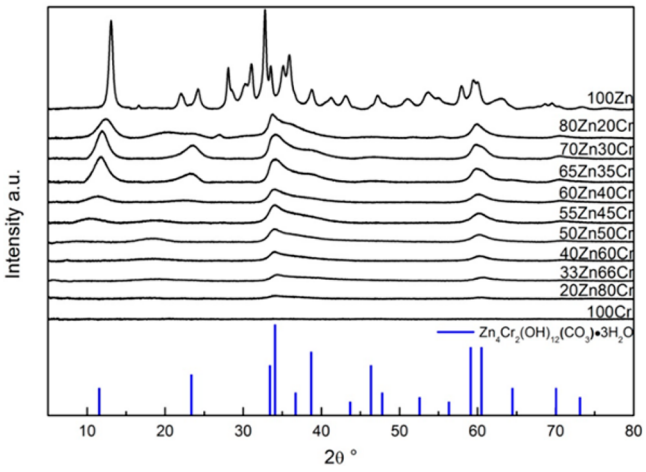

Figure 1. XRD patterns of the hydroxycarbonate precursors.

the reflections can be assigned to zinc hydroxycarbonate. A few unidentified reflections possibly originate from $Zn(OH)_2$ or/and $ZnCO_3$. For the precursors containing both Cr and Zn, the existence of the Zn−Cr hydrotalcite-like phase $Zn_4Cr_2(OH)_{12}CO_3$ can be confirmed by identification of the corresponding characteristic reflections located at 2θ = 34.5° and 2θ = 61.2°.[50,51] With decreasing nominal Zn:Cr ratio from 80:20 to 20:80, these two reflections become broader and their intensity decreases, which indicates that the precursors become more amorphous as more Cr is present. The XRD pattern of 100Cr shows no identifiable reflections at all. With decreasing Zn:Cr ratio, more $Cr(OH)_3$ can be formed during the coprecipitation, which results in a more amorphous state of the precursors. It has to be pointed out that $Cr_2(CO_3)_3$ is not the product of the precipitation of Cr^{3+} using Na_2CO_3 solution.[52]

Figure 2 shows the XRD patterns of the calcined ZnO/Cr_2O_3 catalysts. It can be seen that the hydroxycarbonates with hydrotalcite-like structure were decomposed by calcination at 320 °C for 3 h. The XRD pattern of 100Zn exhibits clear and sharp reflections of ZnO indicating the formation of relatively large ZnO particles. With decreasing Zn:Cr ratio from 100:0 to 70:30, the reflections of ZnO generally become broader and weaker, and a further decrease in the Zn:Cr ratio leads to the disappearance of the ZnO reflections. The $ZnCr_2O_4$ spinel phase is found to exist in the catalysts with the Zn:Cr ratios from 70:30 to 20:80. The catalysts containing high levels of Cr show sharper reflections of $ZnCr_2O_4$ compared with the catalysts containing more Zn. Furthermore, the sharp reflections of Cr_2O_3 can only be found in the XRD pattern of 100Cr. Additionally, a series of small and sharp reflections located between 2θ = 14° and 32° can be observed in the catalysts containing a high amount of Cr, which can be mostly assigned to zinc and sodium chromate. The presence of sodium chromates in the calcined catalyst corresponds to the results obtained by ICP-OES, which show a certain amount of Na

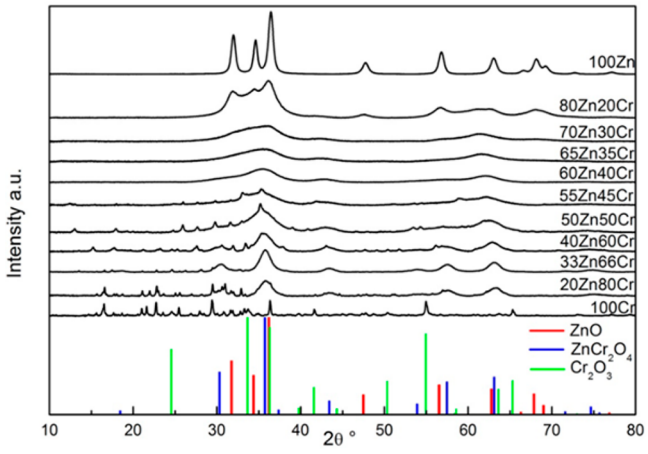

Figure 2. XRD patterns of the calcined ZnO/Cr_2O_3 catalysts.

residue to be present in the catalyst containing excess of Cr. Obviously, the residual Na compounds such as Na_2CO_3 react with Cr_2O_3 and O_2 forming sodium chromates. In addition to the formation of sodium chromates, Cr_2O_3 can also be oxidized yielding $ZnCrO_4$.

The catalysts with a Zn:Cr ratio in the range from 55:45 to 33:66 only exhibit the broad reflections of the $ZnCr_2O_4$ phase in addition to the chromates phases. According to Table 1, a considerable amount of ZnO should be present in these catalysts due to the 1:2 ratio of Zn:Cr in $ZnCr_2O_4$, even if all Cr_2O_3 reacted to form $ZnCr_2O_4$ during the calcination, but no characteristic ZnO reflections were found. The absence of ZnO in the ZnO/Cr_2O_3 catalyst with low Zn:Cr ratio is in agreement with the results reported by Del Piero et al.,[19] who suggested that ZnO can be dissolved in the $ZnCr_2O_4$ spinel to form a nonstoichiometric Zn−Cr spinel. Hence, a small shift of the $ZnCr_2O_4$ reflections is supposed to be detected. The quantity of nonstoichiometric Zn−Cr spinel can be estimated by determination of the lattice parameter of the spinel phase using quantitative XRD analysis.[19,26] However, due to the broad reflections, this method cannot be applied in the present work.

Figure 3 shows the effect of the Zn: Cr ratio on the formation of chromates and spinels during calcination more clearly. After calcination at 250 and 320 °C, the 65Zn catalyst exhibits a series of broad reflections indicating the existence of amorphous material. A further increase in temperature led to the appearance of the sharp reflections of ZnO and $ZnCr_2O_4$. Based on these observation and the XRD patterns of the used catalyst, it can be assumed that the catalyst contains amorphous ZnO and $ZnCr_2O_4$. The 33Zn catalyst shows sharp reflections of zinc chromate at the calcination temperature of 250 °C. At higher calcination temperatures, spinel reflections can be found in the XRD patterns. The differences in the XRD patterns of 65Zn35Cr and 33Zn66Cr at the same calcination temperature provide a strong indication that the Zn:Cr ratio plays a crucial role in the phase composition of the calcined catalyst and the morphology of the each component. For catalysts with high Zn:Cr ratio, amorphous ZnO and spinel are formed during calcination. Considering the stoichiometry of the Zn−Cr hydrotalcite-like compound $Zn_4Cr_2(OH)_{12}(CO_3)$ found in the precursor, it is assumed that for catalysts with Zn:Cr ratios between 100:0 and 66:33, the main phases existing in the precursor are Zn−Cr hydroxycarbonates and $Zn(OH)_2$ or $ZnCO_3$.[53] During calcination hydrotalcite-like Zn−Cr hydrox-

DOI: 10.1021/acscatal.7b01822
ACS Catal. 2017, 7, 7610−7622

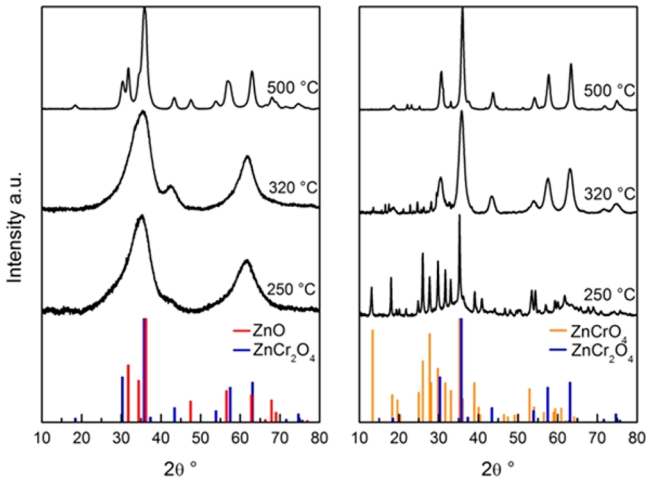

Figure 3. XRD patterns of the ZnO/Cr_2O_3 catalysts with Zn:Cr ratio of 65:35 (left) and 33:66 (right) calcined at 250 °C, 320 and 500 °C for 3 h.

ycarbonate decomposes to form Zn−Cr spinel and ZnO, which is also the product of the decomposition of $Zn(OH)_2$ and $ZnCO_3$. For catalysts with Zn:Cr ratios smaller than 66:33, a considerable amount of $Cr(OH)_3$ is also present in the precursor. Hence, $ZnCrO_4$ was formed by oxidation of Cr_2O_3 in the present of ZnO and O_2. At high temperatures, $ZnCrO_4$ can decompose back to ZnO and spinel with a relatively large particle size. Thus, the higher Cr content the catalyst has, the more $ZnCr_2O_4$ is formed through this pathway, resulting in a lower surface area and more $ZnCrO_4$ in the catalyst.

Figure 4 shows the Raman spectra of the catalysts with different Zn:Cr ratios. The observed Raman modes and data

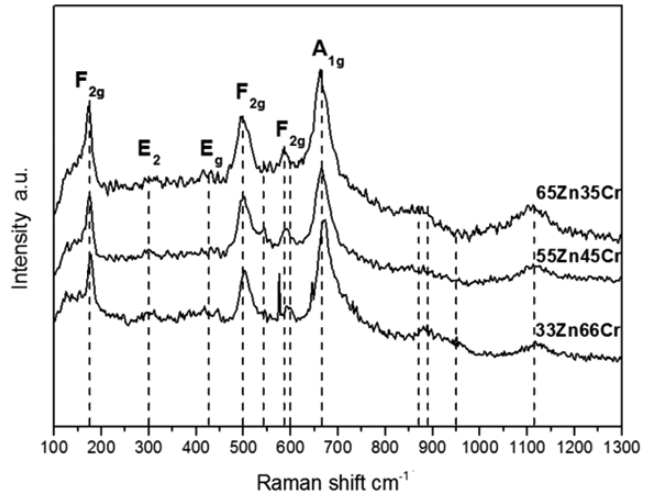

Figure 4. Raman spectra of the ZnO/Cr_2O_3 catalysts with different Zn:Cr ratios.

reported in literature are summarized in Table S1. Based on the selection rules, nondefective $ZnCr_2O_4$ spinel should exhibit three Raman active modes, namely, A_{1g}, E_g, and F_{2g}, which are observed in Figure 4. The sharp peak at 175 cm^{-1} originates from the Zn−O bending vibration of the $ZnCr_2O_4$ spinel. The band with medium intensity located at 499 cm^{-1} and the less intense bands at 599 and 586 cm^{-1} can be assigned to the Cr−O stretching vibration (F_{2g}). The intense band at 666 cm^{-1} is attributed to the symmetric Cr−O stretching vibration of A_{1g} symmetry originating from the CrO_6 groups in the spinel structure. Only weak and broad peaks are found at 300 cm^{-1} belonging to the vibration mode associated with the multiple-phonon scattering processes of ZnO. This observation indicates that for catalysts with Zn:Cr ratios higher than 33:66, part of the additional ZnO is dissolved in $ZnCr_2O_4$ forming the nonstoichiometric Zn−Cr spinel. The bands at around 871, 890, and 950 cm^{-1} are ascribed to the Cr−O stretching vibration of chromates. Catalysts with low Zn:Cr ratio seem to exhibit more intense bands at these positions. This observation is consistent with the XRD results indicating that the formation of chromates during calcination is more severe leading to larger chromate particle sizes for the Cr-rich catalysts.

The XP spectra of the calcined ZnO/Cr_2O_3 catalysts with different Zn:Cr ratios are shown in Figure 5. For all the

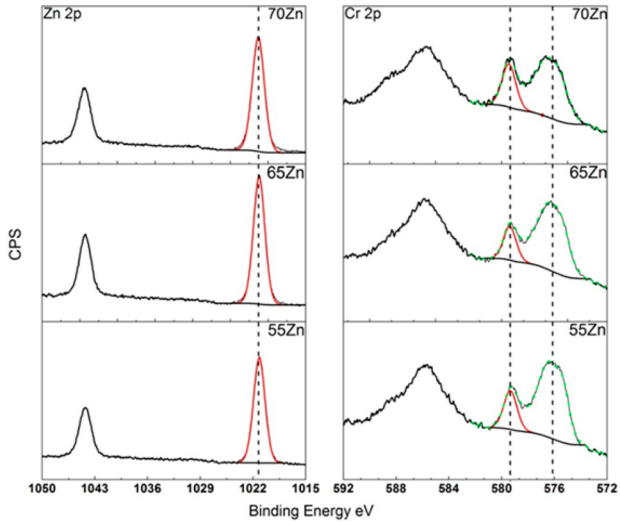

Figure 5. Zn 2p (left) and Cr 2p (right) XP spectra of the calcined ZnO/Cr_2O_3catalysts with different Zn:Cr ratios.

catalysts, the peaks were observed at almost the same position. The Zn $2p_{3/2}$ peak at 1021.2 eV and the Zn $2p_{1/2}$ peak at 1044.2 eV originate from the Zn^{2+} species in the near-surface region of the catalysts. It is not possible to determine whether the Zn^{2+} ions are present in ZnO or $ZnCr_2O_4$ due to their similar peak position.[54] The Cr $2p_{3/2}$ peak at 576.3 eV and the Cr $2p_{1/2}$ peak at 585.9 eV indicate the presence of Cr^{3+} species as in $ZnCr_2O_4$.[55] The Cr $2p_{3/2}$ peak at 579.2 eV confirms the presence of a small amount of surface chromate species resulting from the oxidation during calcination. The atomic Zn:Cr ratio both in the bulk and on the surface of the catalysts are summarized in Table 2. None of the catalysts exhibits

Table 2. Bulk and Surface Composition of the Calcined Catalysts with Different Zn:Cr Ratios before and after Reaction

sample	Zn:Cr ratio before reaction (bulk)	Zn:Cr ratio before reaction (surface)	Zn:Cr ratio after reaction[a] (surface)
70Zn30Cr	71:29	63:37	58:42
65Zn35Cr	67:33	59:41	56:44
55Zn45Cr	57:43	53:47	50:50

[a]At 60 bar and 260−300 °C for 60 h (20 h for each temperature step) with a space velocity of 4800 mL h^{-1} g^{-1}. A syngas mixture with H_2:CO:N_2 = 54:36:10 was used as feed.

DOI: 10.1021/acscatal.7b01822
ACS Catal. 2017, 7, 7610−7622

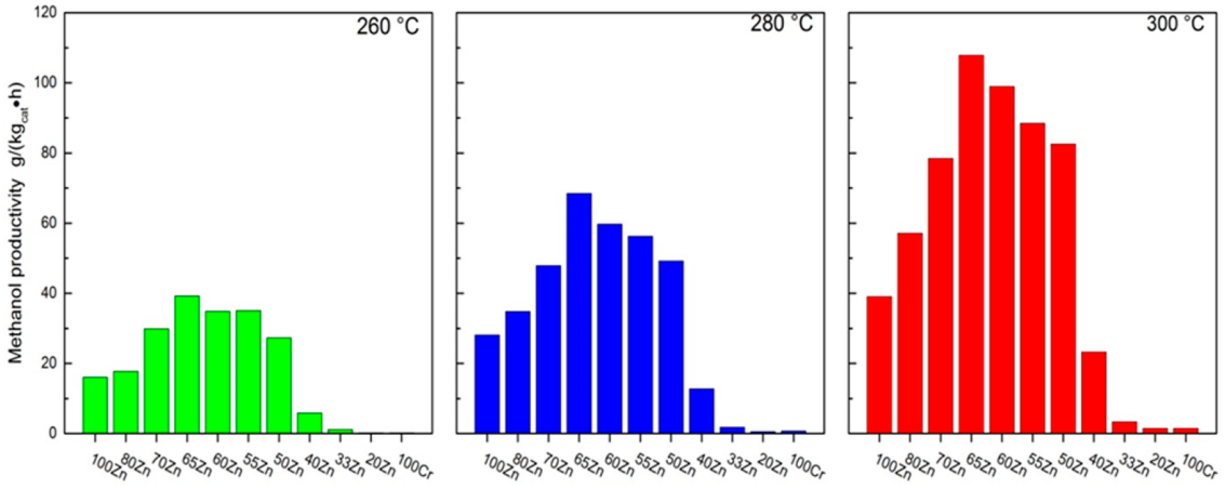

Figure 6. Methanol productivity of catalysts with different Zn:Cr ratios at 260−300 °C, 60 bar H_2:CO:N_2 = 54:36:10 and a flow of 4800 mL h^{-1} g^{-1}.

Table 3. Catalytic Performance of the ZnO/Cr_2O_3 Catalysts with Different Zn:Cr Ratio in Methanol Synthesis[a]

	260 °C			280°			300 °C		
catalyst	X_{CO} (%)	S_{MeOH} (%)	S_{HC}[b] (%)	X_{CO} (%)	S_{MeOH} (%)	S_{HC}[b] (%)	X_{CO} (%)	S_{MeOH} (%)	S_{HC}[b] (%)
100Zn	1.3	52.1	20.4	2.9	40.9	25.0	6.0	27.5	32.3
80Zn20Cr	1.9	46.3	23.2	3.6	41.8	25.3	6.8	34.6	29.6
75Zn25Cr	1.5	79.6	9.6	2.9	66.3	16.3	5.6	56.9	21.1
65Zn35Cr	1.8	86.7	6.3	3.3	77.6	10.0	5.9	75.2	11.3
60Zn40Cr	1.7	81.5	6.8	3.2	76.1	10.9	5.8	69.8	13.2
55Zn45Cr	1.7	82.7	7.9	3.1	72.6	12.4	5.7	63.2	16.8
50Zn50Cr	1.3	86.7	6.6	2.3	87.1	6.2	4.0	83.7	7.2
40Zn60Cr	0.5	46.7	27.1	0.9	55.8	20.7	1.9	53.9	21.1
33Zn66Cr	0.4	13.6	45.1	0.6	13.4	45.9	0.9	14.5	45.1
20Zn80Cr	0.3	3.5	63.8	0.8	4.7	60.0	1.1	7.2	56.1
100Cr	0.2	4.6	66.4	0.5	6.8	65.1	1.2	5.2	67.1

[a] P = 60 bar, H_2:CO:N_2 = 54:36:10, GHSV = 4800 mL h^{-1} g^{-1} [b] Hydrocarbons with carbon numbers of 1−6.

significant zinc enrichment in the near-surface region. Instead, a nonsignificant chromium enrichment of the surface is observed. Therefore, a core−shell structure with a thick amorphous or highly dispersed ZnO shell on $ZnCr_2O_4$ can be excluded. The Zn−Cr spinel is assumed to be the dominant state of Zn^{2+} in the near-surface region. This spinel structure is nonstoichiometric due to the dissolution of ZnO as indicated by the Zn:Cr ratios higher than 1:2 derived from the XPS results.

Figure S2 shows the H_2 TPR profiles of the calcined catalysts with different Zn:Cr ratios. Pure ZnO (100Zn) exhibits no reduction peak, while the ZnO/Cr_2O_3 catalysts with Zn:Cr ratios from 80:20 to 55:45 show a single well-defined reduction peak at about 310 °C. The single reduction peak of 40Zn60Cr and 33Zn66Cr shifts to 353 and 384 °C, respectively. It can be observed that its intensity increases with decreasing Zn:Cr ratio. For 20Zn, three broad reduction peaks located at 457, 512, and 670 °C are found. The H_2 TPR profile of 100Cr consists of overlapping peaks at 576 and 673 °C. In addition, two sharp shoulders are found between 550 and 580 °C. In the literature,[56−58] the single reduction peak for catalysts with Zn:Cr ratios from 80:20 to 40:60 was ascribed to the reduction of the Zn−Cr spinel. Based on the XRD, XPS, and Raman results in the present work, this peak more likely originates from the reduction of zinc chromates. For 40Zn60Cr and 33Zn66Cr, the shift of this reduction peak to the high-temperature region is caused by the larger chromate particle size. The complicated peaks at high temperature for 20Zn80Cr and 100 Cr originate from the reduction of sodium chromates, which can be further confirmed by the XRD results of these samples after the TPR experiments (Figure S3). The observed reflections of sodium chromite, which is the reduction product of sodium chromate, prove the existence of sodium chromate. Furthermore, the total H_2 consumption (Table S2) increases with decreasing Zn:Cr ratio indicating that the catalysts with high levels of Cr contain a higher amount of chromates species.

Catalytic Tests. The effect of the Zn:Cr ratio on the performance of the catalysts was studied in methanol synthesis. The carbon balance for all the catalytic tests was between 99% and 101%. At all three reaction temperatures the highest methanol productivity was achieved with 65Zn35Cr (Figure 6). The selectivities to methanol and the undesired product hydrocarbons as well as the degrees of CO conversion are summarized in Table 3. For all the catalysts, CO conversion increases with increasing reaction temperature, but the rate of hydrocarbon formation increases more rapidly with rising reaction temperature than that of methanol formation resulting in a lower methanol selectivity at 300 °C. The formation of hydrocarbons over ZnO/Cr_2O_3 catalysts has also been observed by Jiao et al.[14] When the reaction temperature was high enough (400 °C), Zn−Cr oxide catalysts prepared by coprecipitation exhibited almost 100% selectivity toward hydrocarbons and CO_2 combined. In contrast to the 100Cr

DOI: 10.1021/acscatal.7b01822
ACS Catal. 2017, 7, 7610−7622

catalyst without Zn, the 100Zn catalyst without Cr achieves a significant methanol productivity. The catalysts with Zn:Cr ratios in the range from 70:30 to 50:50 reach high degrees of conversion, high methanol selectivity, and low selectivity to hydrocarbons in comparison to the catalysts containing an excess of Cr. Generally, a high Cr content leads to high acidity of the catalyst, which favors the formation of hydrocarbons. Water as the coupled product of hydrocarbon formation further enhances the formation of CO_2. As a result of the enhanced formation of both hydrocarbons and CO_2, the selectivity to methanol significantly decreases.

Furthermore, the high content of Na residue may also play an important role in the low conversion and high selectivity toward hydrocarbons for the catalysts containing excess of Cr. As shown in Table 1, with decreasing Zn:Cr ratio from 50:50 to 0:100, the content of the Na residue increases drastically leading to the formation of more chromate species, which further results in the rapid decrease in surface area. As a result, the degree of conversion for these catalysts decreases with increasing Na content. In addition, the selectivity toward high products also significantly increases with increasing Na content. This observation corresponds to the promoting effect of alkali metals on the formation of long-chain products, which has been reported in both Fischer–Tropsch synthesis[59,60] and higher alcohol synthesis.[54,55] Additionally, a series of Na-free catalysts was synthesized by using $(NH_4)_2CO_3$ as the precipitation reagent, while other preparation and test conditions were not changed. As shown in Figure S4, the Na residue was confirmed to cause the drastic decrease in surface area. Correspondingly, for catalysts with Zn:Cr < 50:50, the application of a Na-free precipitation reagent can significantly improve the methanol productivity (Figure S5) due to the absence of sodium chromate species (Figure S6). More importantly, the catalyst with Zn:Cr = 65:35 still exhibits the highest methanol productivity, and the dependence of catalytic activity of the catalyst on the Zn:Cr ratio is not significantly changed.

Characterization of the Catalysts after Methanol Synthesis. The XRD patterns of the ZnO/Cr_2O_3 catalysts after reaction are shown in Figure S7. Compared with the fresh catalysts (Figure 2), the used catalysts exhibit slightly sharper reflections, which indicate a small increase of the particle size, but no severe sintering. Analogous to the fresh catalysts, the used catalysts also exhibit a change of the dominating phase from ZnO to $ZnCr_2O_4$ with decreasing Zn:Cr ratio. Correspondingly, under reaction conditions neither ZnO nor $ZnCr_2O_4$ were decomposed or transformed into other phases. Furthermore, no characteristic reflections of Cr_2O_3 can be found in all the XRD patterns for the catalyst containing both Zn and Cr, presumably due to the small particle size of Cr_2O_3. For the catalysts with an excess of Cr, the small sharp reflections of the chromates phase can no longer be seen indicating the reduction of chromates during methanol synthesis. For 100Cr containing the highest level of residual Na, the sharp reflections suggest the presence of Na-containing compounds. Figure 7 demonstrates more clearly that after reaction weak reflections of ZnO can be identified for the Zn:Cr = 65:35 and 60:40 catalysts. With further decreasing Zn:Cr ratio, the catalysts only exhibit more intensive spinel reflections. The XP spectra of the ZnO/Cr_2O_3 catalysts after reaction are shown in Figure S8. The Zn $2p_{3/2}$ peak at 1021.1 eV and the broad Cr $2p_{3/2}$ peak at 576.2 eV reveal that after reaction Zn^{2+} and Cr^{3+} are still the primary states of Zn and Cr species in the near-surface region of the catalyst. The peak

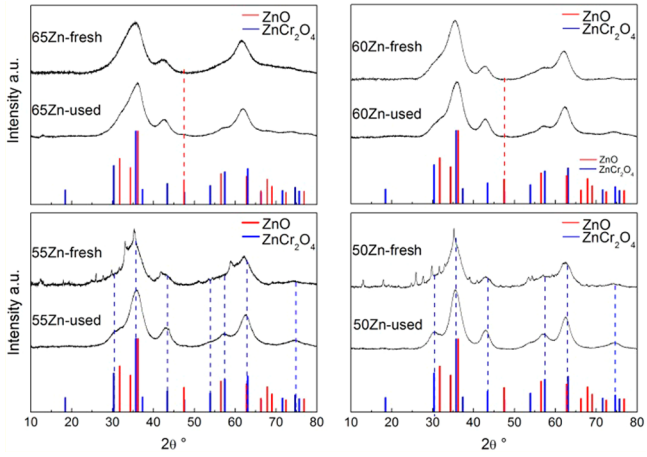

Figure 7. XRD patterns of the ZnO/Cr_2O_3 catalysts with Zn:Cr ratios from 65:35 to 50:50 before and after reaction at 60 bar and 260–300 °C for 60 h (20 h for each temperature step) with a space velocity of 4800 mL h^{-1} g^{-1}. A syngas mixture with H_2:CO:N_2 = 54:36:10 was used as feed.

originating from the surface chromate species can no longer be observed indicating that these species were fully reduced during the catalytic tests, which is in a good agreement with the XRD results of the catalyst after reaction (Figures S7 and 7). In no case was there significant Zn enrichment observed in the near-surface region of the catalysts after reaction (Table 2). These observations support the hypothesis that the nonstoichiometric Zn–Cr spinel is the active phase in ZnO/Cr_2O_3 catalyst for methanol synthesis.

Density Functional Theory Calculations. To aid in determining the active phase of the ZnO/Cr_2O_3 methanol synthesis catalyst, we have investigated different compositions of ZnO/Cr_2O_3 using density functional theory calculations. We first consider Cr doping in bulk ZnO and in the nonpolar (10–10) ZnO surface by replacing Zn^{2+} lattice cation sites with Cr^{3+} cations at different concentrations. The first Cr^{3+} cations substitutionally dope a Zn^{2+} cation site for a 2% doping concentration in either bulk or surface. However, for larger concentrations of Cr^{3+}, different Zn^{2+} substitutional sites are explored to determine the relative distribution of Cr in the ZnO structures. Once the lowest-energy configurations for different concentrations are established, then oxygen vacancy formation is examined by removing different oxygen atoms from the doped structures to determine the lowest oxygen vacancy formation energy. This procedure is followed for all doped systems.

The lowest-energy configurations for the Cr distributions for 1–10% doping in bulk ZnO and the (10–10) surface of ZnO, and the positions of the oxygen vacancies are shown in the Supporting Information, Figures S9 and S10. The lowest oxygen vacancy energies are shown as a function of the Cr doping concentration in Figure 8 to examine the effect of bulk and surface Cr doping of ZnO on the reducibility. For Cr doping in bulk ZnO, the oxygen vacancy formation energy increases with increasing Cr doping concentration up to 4% and remains constant thereafter, showing no change up to 10%. Larger doping concentrations beyond this value are expected to show no enhancement in the oxygen vacancy formation energy. The oxygen vacancy formation energy for Cr doping in the ZnO surface follows a similar trend to the bulk, increasing up to

DOI: 10.1021/acscatal.7b01822
ACS Catal. 2017, 7, 7610–7622

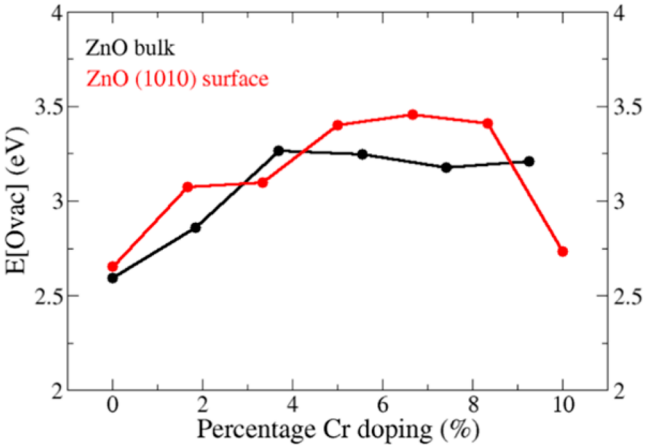

Figure 8. Oxygen vacancy formation energies for Cr doping in the ZnO bulk and the (10−10) surface.

8% Cr doping, while at 10% the oxygen vacancy formation energy is similar to the undoped surface.

Computed Bader charges and spin magnetizations for the Cr cations are between 10.65 and 10.70 electrons and 3 spins when Cr is doped into ZnO. These are typical of Cr^{3+} cations, and this oxidation state is maintained up to 10% Cr doping. The formation of an oxygen vacancy reduces Zn cations, regardless of the Cr doping concentration.

Doping both the ZnO bulk and surface with Cr does not improve the oxygen vacancy formation as the calculated formation energies are always larger than the undoped structures. The origin of this result is that the Cr^{3+} dopant on a Zn^{2+} site introduces an extra electron into the system, and as the formation of an oxygen vacancy is also a reducing process (releasing two electrons into the system), it becomes increasingly more difficult to form oxygen vacancies with increasing the number of Cr dopants in the structures. Therefore, the Cr-doped ZnO structure as a possible composition with an excess of Zn over Cr cannot be the active phase for methanol synthesis, as the formation of active oxygen vacancies has a high energy cost at the optimum experimentally determined ratio of 65:35 Zn:Cr.

The formation of oxygen vacancies was investigated in the $ZnCr_2O_4$ spinel bulk and the (100) surface in a similar fashion. The (100) surface is studied as recent work indicates that this is the stable surface of the Zn−Cr spinel rather than the (111) surface described in older studies using interatomic potentials.[61] The calculated oxygen vacancy formation energy for the bulk $ZnCr_2O_4$ spinel is +4.41 eV, which is larger than ZnO and Cr-doped ZnO. Doping the $ZnCr_2O_4$ spinel with excess Zn replaces an octahedrally coordinated Cr^{3+} cation with a Zn^{2+} cation which is a lower valence dopant. Two Zn^{2+} must then be incorporated into the spinel structure (forming two holes on neighboring oxygen atoms) with charge compensation by oxygen vacancy formation, described as a $[2Zn'_{Cr} + V_O^{\cdot}]$ species in Kröger−Vink notation; this is similar to Zn-doped bulk Cr_2O_3.[36] The calculated oxygen vacancy formation energy for Zn doping in the spinel is +3.49 eV, showing an improvement over the undoped spinel bulk, but the energy cost is higher than for ZnO. Upon further Zn doping of the bulk spinel, the oxygen vacancy formation energy increases.

In studying the formation of oxygen vacancies in the (100) surface of the $ZnCr_2O_4$ spinel, we examined surface and subsurface oxygen vacancies and we find that surface oxygen vacancy formation is preferred with a calculated formation energy of +1.59 eV. This is significantly lower than oxygen vacancy formation in the Cr-doped ZnO systems and the spinel bulk, indicating that the spinel surface is more reducible.

Zn doping in the (100) $ZnCr_2O_4$ spinel surface is investigated to model the incorporation of excess Zn in the nonstoichiometric methanol catalyst described in the experimental studies. Similar to the spinel bulk, the Zn^{2+} dopants replace Cr^{3+} cations on their lattice sites and are compensated by formation of charge-balancing oxygen vacancies; Table 4

Table 4. Calculated Formation Energies for Compensating, *E*[comp], and Reducing, *E*[reducing], Oxygen Vacancies for Different Concentrations of Zn in the $ZnCr_2O_4$ Spinel Surface

	E[comp] (eV)	*E*[reducing] (eV)
0% Zn doping (30% Zn content)	---	+1.59
6.66% Zn doping (40% Zn content)	+0.41	+2.85
13.33% Zn doping (46.66% Zn content)	−0.05	+2.02
20% Zn doping (53.33% Zn content)	−0.02	+1.58
26.67% Zn doping (60% Zn content)	−0.25	+1.55

shows that the formation energies for the charge compensating oxygen vacancies are close to 0 eV, which is typical for spontaneous formation of a charge compensating oxygen vacancy. In the (100) spinel surface, Zn dopants can substitute at surface or subsurface Cr sites or in the bulk-like region of the surface slab, and we examined these sites for Zn doping. We also investigate the possible compensating oxygen vacancy sites. Once the lowest-energy charge balanced Zn doping configuration is established, the reducing oxygen vacancy is investigated to determine the reducibility of the surface compared to the undoped surface. Zn doping contents up to 60% Zn are studied, which is close to the optimum experimental Zn:Cr ratio.

The calculated formation energies for the reducing oxygen vacancies are shown in Table 4. These oxygen vacancy formation energies show that initial Zn doping at 6.66% increases the vacancy formation energy. However, further Zn doping of the surface significantly enhances oxygen vacancy formation in the surface and thus increases the surface reducibility. For 20−26.67% Zn doping, the oxygen vacancy formation energies are similar to the undoped spinel surface.

The structures for the (100) surface of the spinel with varying Zn content are shown in Figure 9. The Zn^{2+} dopants preferentially replace all the available surface Cr^{3+} lattice sites up to 46.66% Zn content (Figure 9c). Further Zn doping then replaces Cr cation sites in the subsurface layer, and for 60% Zn content (26.66% doping), all Cr cations in the surface and subsurface layers have been replaced by Zn cations. The compensating oxygen vacancies are preferentially removed from the surface and subsurface regions, resulting in a 1:1 ratio of Zn:O in this region in which all Zn have a 2+ oxidation state. **This structure has the appearance of a thin amorphous ZnO layer on the $ZnCr_2O_4$ spinel structure, which accommodates the excess Zn on the original Cr^{3+} sites and has an overall stoichiometry similar to experiment. This region contains undercoordinated Zn and O sites on the surface and promotes oxygen vacancy formation at the surface.** Thus, we can unravel, for the first time, the precise atomic level nature of the active, Zn-rich $ZnCr_2O_4$ spinel catalyst.

DOI: 10.1021/acscatal.7b01822
ACS Catal. 2017, 7, 7610−7622

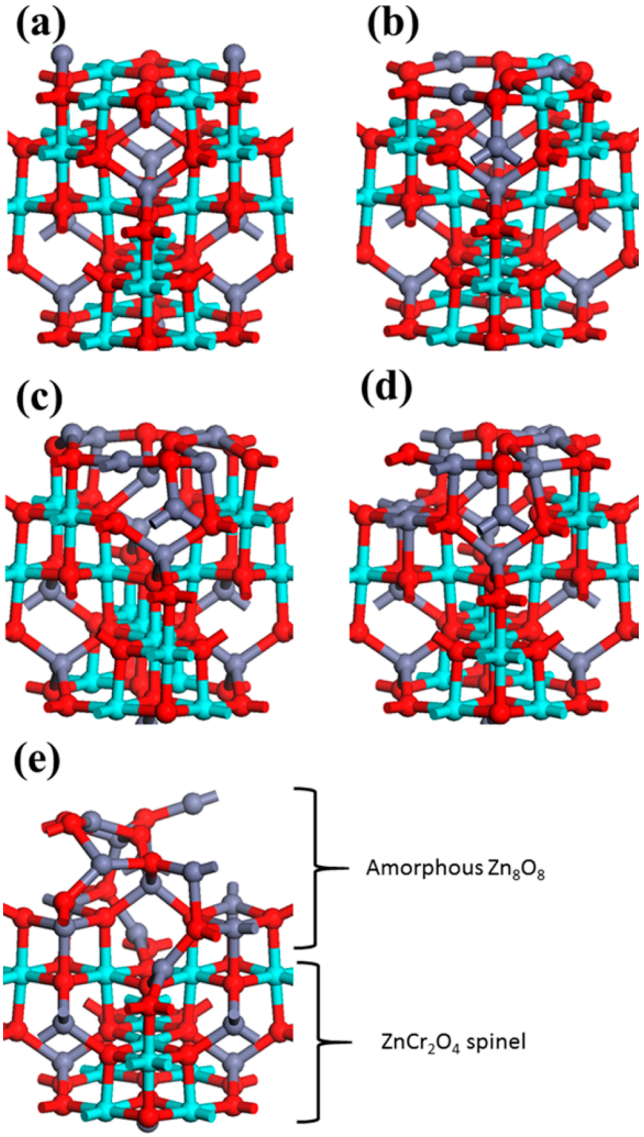

Figure 9. Calculated local structure for (a) 0%, (b) 6.67%, (c) 13.33%, (d) 20%, and (e) 26.67% Zn doping in the (100) surface of the $ZnCr_2O_4$ spinel.

We note from Table 4 that both the stoichiometric and the Zn-excess spinel structures have low formation energies for the reducing oxygen vacancy. However, this process is not the only important process in the methanol synthesis. The initial adsorption and activation of CO and hydrogen on the catalyst surface are also important. Figure 10 shows the adsorption structures for a H atom and the CO molecule adsorbed on the stoichiometric and Zn-excess spinel surface. On $ZnCr_2O_4$, the computed H and CO adsorption energies are −1.18 eV and −2.08 eV, relative to $1/2H_2$ and free CO. With excess Zn, the corresponding adsorption energies are −0.99 eV and −1.14 eV for H and CO. On both surfaces, CO and H adsorb favorably, and the further reaction of the molecules to hydrogenate CO to methanol depends on the strength of the initial adsorption. We therefore propose that the weaker, but still favorable, H and CO adsorption energies on the nonstoichiometric $ZnCr_2O_4$ allow for more favorable hydrogenation of CO, thus enhancing the production of methanol.

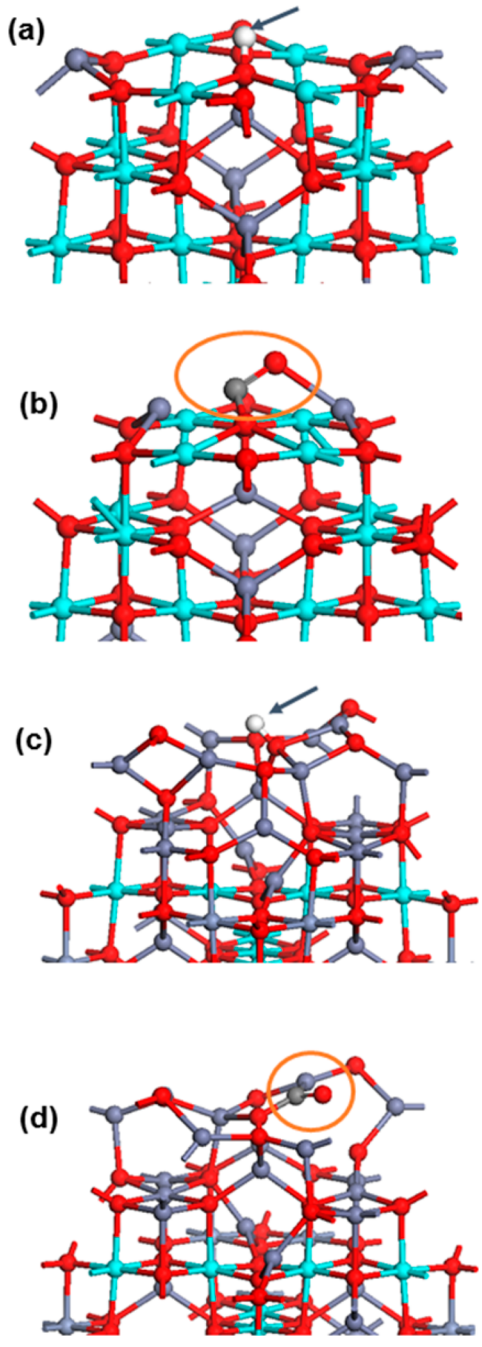

Figure 10. Calculated atomic structure for (a) H atom adsorption and (b) CO adsorption on the stoichiometric $ZnCr_2O_4$ spinel. Panels (c) and (d) show the atomic structure for H atom and CO adsorption on the Zn-rich $ZnCr_2O_4$ spinel from our model of the Zn-rich $ZnCr_2O_4$ spinel, which is shown in Figure 9e. In this figure, H is the white sphere, C is the gray sphere. The arrow and the orange ring indicate the adsorbates.

4. DISCUSSION

In recent literature, the nonstoichiometric Zn−Cr spinel has been repeatedly reported as the active phase of ZnO/Cr_2O_3 catalysts applied in methanol synthesis,[18−22,26,55−58] which originates from the dissolution of excess ZnO in $ZnCr_2O_4$. In the present work, the diffraction patterns of the calcined Zn-rich catalysts with Zn:Cr ratios in the range from 65:35 to 50:50 shown in Figure 2 do not indicate the presence of ZnO, although a considerable amount of ZnO should be present in

DOI: 10.1021/acscatal.7b01822
ACS Catal. 2017, 7, 7610−7622

these catalysts according to their composition. In the Raman spectra shown in Figure 4, the weak and broad band originating from the multiple-phonon scattering processes of ZnO further confirms that the amount of detected ZnO was always smaller than that expected for a simple phase mixture of ZnO and $ZnCr_2O_4$ with Zn:Cr ratios in the range from 65:35 to 50:50. The existence of a substantial amount of highly dispersed or amorphous ZnO, which is not detectable by XRD and Raman spectroscopy, has been excluded by the XPS results, in which no Zn enrichment was observed for the calcined catalysts before or after reaction (Table 2). All these observations indicate the presence of nonstoichiometric Zn−Cr spinel formed by the dissolution of ZnO in $ZnCr_2O_4$. For catalysts even with a Zn:Cr ratio of 65:35, essentially all Zn^{2+} ions are present in the nonstoichiometric Zn−Cr spinel due to the high solubility of ZnO in $ZnCr_2O_4$.[23,26] According to the DFT results, this Zn-rich nonstoichiometric Zn−Cr spinel system is in fact composed of a thin ZnO-like layer supported on the spinel surface that results from replacement of surface and subsurface Cr cations with Zn, rather than bulk doping of the spinel.

In spite of the absence of bulk ZnO, these catalysts achieve high activity in methanol synthesis, suggesting the nonstoichiometric Zn−Cr spinel to be the active phase. After reaction weak reflections of ZnO are found for the catalysts with Zn:Cr ratios of 65:35 and 60:40 (Figure 8), indicating a minor increase of the amount of ZnO in the catalyst. This segregation seems to be correlated with the slight deactivation of the catalysts with time on stream, during which a small amount of nonstoichiometric Zn−Cr spinel changed toward its stoichiometric form accompanied by the formation of ZnO.[19] Furthermore, as shown in Figure 3, high calcination temperatures up to 500 °C can accelerate the segregation of the nonstoichiometric spinel structure resulting in the stoichiometric Zn−Cr spinel $ZnCr_2O_4$ and crystalline ZnO.[19,55]

The Zn:Cr ratio can significantly influence the amount of the catalytically active nonstoichiometric Zn−Cr spinel in the catalyst due to its effect on the structure of the coprecipitated catalyst precursor. In Figure 1, the reflections of $Zn_4Cr_2(OH)_{12}CO_3$ can be observed for Zn:Cr ratios in the range from 80:20 to 20:80, indicating that the formation of this hydrotalcite-like Zn−Cr hydroxycarbonate is favored during coprecipitation. Due to the stoichiometric constraint of Zn:Cr = 2:1 in $Zn_4Cr_2(OH)_{12}CO_3$, the highest amount of $Zn_4Cr_2(OH)_{12}CO_3$ can be obtained with Zn:Cr = 65:35, and a further increase or decrease in the Zn:Cr ratio leads to the formation of Zn-rich hydroxycarbonates and amorphous $Cr(OH)_3$, respectively. As shown in Figure 2, $Zn_4Cr_2(OH)_{12}CO_3$ decomposes during calcination forming ZnO and $ZnCr_2O_4$. It is worth noting that the formation of $ZnCr_2O_4$ via a solid-state reaction of ZnO and Cr_2O_3 would require much high temperatures. Hence, $Zn_4Cr_2(OH)_{12}CO_3$ is assumed to be the major source for $ZnCr_2O_4$ under the applied mild calcination conditions in synthetic air at 320 °C for 3 h.[62] As a result, the catalyst with a ratio of Zn:Cr = 65:35 presumably contains the highest amount of $ZnCr_2O_4$, implying that the highest amount of nonstoichiometric spinel can be formed. Indeed, the catalyst with Zn:Cr = 65:35 exhibits the highest productivity in methanol synthesis. With a further increase in the Zn:Cr ratio from 65:35, the catalyst contain less $ZnCr_2O_4$, and the larger amount of Zn-containing hydroxycarbonate phases favors the formation of ZnO. The important role of $Zn_4Cr_2(OH)_{12}CO_3$ is that both Zn^{2+} and Cr^{3+} can exist in the same phase, which is beneficial for the formation of Zn−Cr nonstoichiometric spinel during calcination.

DFT calculations confirm for the first time that the active phase of the catalyst is not the ZnO structure doped with Cr, as the formation of oxygen vacancies is not favorable, and thus, this composition will not be active for methanol synthesis. The calculations show that the (100) surface of the $ZnCr_2O_4$ spinel has favorable oxygen vacancy formation energies, which has been shown to be a key property for methanol synthesis. For the nonstoichiometric spinel structure with excess Zn (60%) content, the nonstoichiometric surface is terminated by an amorphous-like thin layer of ZnO. This is the active phase for the methanol synthesis catalyst, as it has a low oxygen vacancy formation energy, favorable, but not too strong H and CO adsorption energies and therefore has activity required for methanol synthesis.

The drastic loss of activity for the catalysts containing an excess of chromium can be explained analogously. Due to stoichiometric constraints, the higher Cr content leads to less hydrotalcite-like $Zn_4Cr_2(OH)_{12}CO_3$ during coprecipitation and more Cr being presumably present in the form of amorphous $Cr(OH)_3$. Furthermore, due to the acidity of $Cr(OH)_3$, the sodium residues cannot be completely removed by washing after coprecipitation (Table 1). Hence, after calcination, the amount of amorphous ZnO and spinel generated from decomposition of the $Zn_4Cr_2(OH)_{12}CO_3$ decreases, and more Cr_2O_3 formed by decomposition of $Cr(OH)_3$ can react with ZnO or sodium residues in the present of O_2 to form chromates (Figure 2). This competitive reaction can negatively influence the formation of the nonstoichiometric spinel, and the formed chromate can partially decompose or be reduced to form spinel again, but with high crystallinity and large particle sizes. Further studies are in progress aiming at further increasing the amount of nonstoichiometric Zn−Cr spinel by improving the precipitation and post-treatment conditions and at identifying the amorphous thin ZnO layer on the Zn−Cr spinel by low-energy ion scattering spectroscopy and high-resolution transmission electron microscopy. Furthermore, since the formation of the Zn−Cr nonstoichiometric spinel increases the amount of Zn^{2+} cations located at octahedral sites, X-ray absorption spectroscopy may be a suitable characterization method to determine its amount.

5. CONCLUSIONS

A series of ZnO/Cr_2O_3 catalysts with different Zn:Cr ratios was prepared by coprecipitation at pH 7 and calcination at 320 °C. The Zn:Cr ratio was found to have a significant influence on the structural and catalytic properties. The catalysts with Zn:Cr ratios between 70:30 and 55:45 had relatively high specific surface areas of about 100 $m^2\ g^{-1}$, whereas the small specific surface area of Cr-rich catalysts is mainly attributed to the formation of chromates during calcination in the presence of sodium residues after coprecipitation. XRD, XPS, and Raman results confirm that the nonstoichiometric Zn−Cr spinel is present in the calcined ZnO/Cr_2O_3 catalysts. The catalyst with a Zn:Cr ratio of 65:35 exhibits the highest methanol productivity of about 105 g $(kg_{cat}\cdot h)^{-1}$ at 300 °C. This ratio corresponds to the stoichiometric Zn:Cr ratio of the hydrotalcite-like precursor $Zn_4Cr_2(OH)_{12}CO_3$ formed during coprecipitation. It is suggested that 65:35 is the optimal Zn:Cr ratio yielding the highest amount of $Zn_4Cr_2(OH)_{12}CO_3$, which further decomposes during calcination forming the highest amount of the nonstoichiometric Zn−Cr spinel as

DOI: 10.1021/acscatal.7b01822
ACS Catal. 2017, 7, 7610−7622

active phase of ZnO/Cr_2O_3 catalysts applied in methanol synthesis. Density functional theory calculations have characterized the nonstoichiometric Zn−Cr catalyst with excess Zn as an amorphous ZnO layer supported on the $ZnCr_2O_4$ spinel structure, thus confirming this system as the active methanol synthesis catalyst with the lowest formation energy for oxygen vacancies.

■ ASSOCIATED CONTENT

Supporting Information

The Supporting Information is available free of charge on the ACS Publications website at DOI: 10.1021/acscatal.7b01822.

Flow scheme of the high-pressure setup; H_2 TPR profiles and H_2 consumption; observed Raman modes; results obtained with $(NH_4)_2CO_3$ as precipitating agent; XRD patterns and XP spectra after reaction; various tested sites for Cr doping in ZnO by DFT+U calculations (PDF)

■ AUTHOR INFORMATION

Corresponding Authors

*E-mail: michael.nolan@tyndall.ie.
*E-mail: muhler@techem.rub.de.

ORCID

John J. Carey: 0000-0003-1835-9364
Michael Nolan: 0000-0002-5224-8580
Martin Muhler: 0000-0001-5343-6922

Notes

The authors declare no competing financial interest.

■ ACKNOWLEDGMENTS

This work was supported by the European FP7 NMP 2013 project BIOGO (grant no: 604296) (Catalytic partial oxidation of biogas and reforming of pyrolysis oil for synthetic gas production and conversion into fuels, www.biogo.eu). J.J.C and M.N would like to acknowledge use of the Science Foundation Ireland (SFI) funded computational resources at Tyndall and at the Irish Centre for High End Computing (ICHEC), and support from the COST action CM1104.

■ REFERENCES

(1) Wender, I. *Catal. Rev.: Sci. Eng.* **1984**, *26*, 303−321.
(2) Calkins, W. H. *Catal. Rev.: Sci. Eng.* **1984**, *26*, 347−358.
(3) Mittasch, A.; Schneider, C. U.S. Patent No. US1201850, 1916.
(4) Mittasch, A.; Pier, M.; Winkle, K. U.S. Patent No. US1558559, 1925.
(5) Mittasch, A.; Pier, M. U.S. Patent No. US1569775, 1926.
(6) Gallagher, J.; Kidd, J. Patent No. GB1159035, 1969.
(7) Cornthwaite, D. Patent No. GB1296212, 1972.
(8) Natta, G. In *Catalysis*; Emmet, P. H., Eds.; Reinhold Publishing Corporation: New York, 1955; Vol. 3, p 349.
(9) Riva, A.; Trifiro, F.; Vaccari, A.; Busca, G.; Mintchev, L.; Sanfilippo, D.; Manzatti, W. *J. Chem. Soc., Faraday Trans. 1* **1987**, *83*, 2213−2225.
(10) Epling, W. S.; Hoflund, G. B.; Hart, W. M.; Minahan, D. M. *J. Catal.* **1997**, *169*, 438−446.
(11) Epling, W. S.; Hoflund, G. B.; Hart, W. M.; Minahan, D. M. *J. Catal.* **1997**, *172*, 13−23.
(12) Minahan, D. M.; Epling, W. S.; Hoflund, G. B. *Appl. Catal., A* **1998**, *166*, 375−385.
(13) Ereña, J.; Arandes, J. M.; Bilbao, J.; Aguayo, A. T.; de Lasa, H. I. *Ind. Eng. Chem. Res.* **1998**, *37*, 1211−1219.
(14) Jiao, F.; Li, J.; Pan, X.; Xiao, J.; Li, H.; Ma, H.; Wei, M.; Pan, Y.; Zhou, Z.; Li, M.; Miao, S.; Li, J.; Zhu, Y.; Xiao, D.; He, T.; Yang, J.; Qi, F.; Fu, Q.; Bao, X. *Science* **2016**, *351*, 1065−1068.
(15) Cryder, D. S.; Frolich, P. K. *Ind. Eng. Chem.* **1929**, *21*, 867−871.
(16) Boccuzzi, F.; Garrone, E.; Zecchina, A.; Bossi, A. *J. Catal.* **1978**, *51*, 160−168.
(17) Kung, H. H. *Catal. Rev.: Sci. Eng.* **1980**, *22*, 235−259.
(18) Kurtz, M.; Strunk, J.; Hinrichsen, O.; Muhler, M.; Fink, K.; Meyer, B.; Wöll, C. *Angew. Chem., Int. Ed.* **2005**, *44*, 2790−2794.
(19) Piero, G. D.; Trifiro, F.; Vaccari, A. *J. Chem. Soc., Chem. Commun.* **1984**, 656−658.
(20) Bertoldi, M.; Fubini, B.; Giamello, E.; Busca, G.; Trifiro, F.; Vaccari, A. *J. Chem. Soc., Faraday Trans. 1* **1988**, *84*, 1405−1421.
(21) Giamello, E.; Fubini, B.; Bertoldi, M.; Busca, G.; Vaccari, A. *J. Chem. Soc., Faraday Trans. 1* **1989**, *85*, 237−249.
(22) Riva, A.; Trifiro, F.; Vaccari, A.; Mintchev, L.; Busca, G. *J. Chem. Soc., Faraday Trans. 1* **1988**, *84*, 1423−1435.
(23) Grimes, R. W.; Binks, D. J.; Lidiard, A. B. *Philos. Mag. A* **1995**, *72*, 651−668.
(24) Bone, W. A. *Trans. Inst. Chem. Eng.* **1930**, *8*, 98−106.
(25) Molstad, M. C.; Dodge, B. F. *Ind. Eng. Chem.* **1935**, *27*, 134−140.
(26) Errani, E.; Trifiro, F.; Vaccari, A.; Richter, M.; Del Piero, G. *Catal. Lett.* **1989**, *3*, 65−72.
(27) Bradford, M. C. J.; Konduru, M. V.; Fuentes, D. X. *Fuel Process. Technol.* **2003**, *83*, 11−25.
(28) Perdew, J. P.; Yue, W. *Phys. Rev. B: Condens. Matter Mater. Phys.* **1986**, *33*, 8800−8802.
(29) Perdew, J. P.; Burke, K.; Ernzerhof, M. *Phys. Rev. Lett.* **1996**, *77*, 3865−3868.
(30) Kresse, G.; Furthmüller. *Comput. Mater. Sci.* **1996**, *6*, 15−50.
(31) Kresse, G.; Furthmüller. *Phys. Rev. B: Condens. Matter Mater. Phys.* **1996**, *54*, 11169−11185.
(32) Kresse, G.; Joubert, D. *Phys. Rev. B: Condens. Matter Mater. Phys.* **1999**, *59*, 1758−1775.
(33) Dudarev, S. L.; Liechtenstein, A. I.; Castell, M. R.; Briggs, G. A. D.; Sutton, A. P. *Phys. Rev. B: Condens. Matter Mater. Phys.* **1997**, *56*, 4900−4908.
(34) Dudarev, S.; Botton, G.; Savrasov, S.; Humphreys, C.; Sutton, A. *Phys. Rev. B: Condens. Matter Mater. Phys.* **1998**, *57*, 1505−1509.
(35) Rohrbach, A.; Hafner, J.; Kresse, G. *Phys. Rev. B: Condens. Matter Mater. Phys.* **2004**, *70*, 125426.
(36) Carey, J. J.; Legesse, M.; Nolan, M. *J. Phys. Chem. C* **2016**, *120*, 19160−19174.
(37) Murnaghan, F. *Proc. Natl. Acad. Sci. U. S. A.* **1944**, *30*, 244−247.
(38) Monkhorst, H. J.; Pack, J. D. *Phys. Rev. B* **1976**, *13*, 5188−5192.
(39) Kemei, M. C.; Barton, P. T.; Moffitt, S. L.; Gaultois, M. W.; Kurzman, J. A.; Seshadri, R.; Suchomel, M. R.; Kim, Y.-I. *J. Phys.: Condens. Matter* **2013**, *25*, 326001.
(40) Reeber, R. R. *J. Appl. Phys.* **1970**, *41*, 5063−5066.
(41) Carey, J. J.; Nolan, M. *Appl. Catal., B* **2016**, *197*, 324−336.
(42) Carey, J. J.; Nolan, M. *Catal. Sci. Technol.* **2016**, *6*, 3544−3558.
(43) Nolan, M. *J. Phys. Chem. C* **2011**, *115*, 6671−6681.
(44) Iwaszuk, A.; Nolan, M. *J. Phys.: Condens. Matter* **2011**, *23*, 334207.
(45) Henkelman, G.; Arnaldsson, A.; Jónsson, H. *Comput. Mater. Sci.* **2006**, *36*, 354−360.
(46) Sanville, E.; Kenny, S. D.; Smith, R.; Henkelman, G. *J. Comput. Chem.* **2007**, *28*, 899−908.
(47) Tang, W.; Sanville, E.; Henkelman, G. *J. Phys.: Condens. Matter* **2009**, *21*, 084204.
(48) Music, S.; Maljkovic, M.; Popovic, S.; Trojko, R. *Croat. Chem. Acta.* **1999**, *72*, 789−802.
(49) Rai, D.; Sass, B. M.; Moore, D. A. *Inorg. Chem.* **1987**, *26*, 345−349.
(50) Parida, K.; Mohapatra, L. *Dalton Trans.* **2012**, *41*, 1173−1178.
(51) del Arco, M.; Rives, V.; Trujillano, R.; Malet, P. *J. Mater. Chem.* **1996**, *6*, 1419−1428.

DOI: 10.1021/acscatal.7b01822
ACS Catal. 2017, 7, 7610−7622

(52) Motzer, W. E. In *Chromium(VI) Handbook*; Guertin, J., Jacobs, J. A., Avakian, C. P., Eds.; CRC Press: Boca Raton, 2004; p 23.
(53) Choudhary, V. R.; Chaudhari, P. A.; Narkhede, V. S. *Catal. Commun.* **2003**, *4*, 171−175.
(54) Epling, W. S.; Hoflund, G. B.; Minahan, D. M. *J. Catal.* **1998**, *175*, 175−184.
(55) Tian, S.; Wang, S.; Wu, Y.; Gao, J.; Bai, Y.; Wang, P.; Xie, H.; Han, Y.; Tan, Y. *J. Mol. Catal. A: Chem.* **2015**, *404*, 139−147.
(56) Tan, L.; Yang, G.; Yoneyama, Y.; Kou, Y.; Tan, Y.; Vitidsant, T.; Tsubaki, N. *Appl. Catal., A* **2015**, *505*, 141−149.
(57) Tian, S.; Wang, S.; Wu, Y.; Gao, J.; Wang, P.; Xie, H.; Yang, G.; Han, Y.; Tan, Y. *Catal. Sci. Technol.* **2016**, *6*, 4105−4115.
(58) Tian, S.; Wang, S.; Wu, Y.; Gao, J.; Xie, H.; Li, X.; Yang, G.; Han, Y.; Tan, Y. *RSC Adv.* **2015**, *5*, 89273−89281.
(59) Ngantsoue-Hoc, W.; Zhang, Y.; O'Brien, R. J.; Luo, M.; Davis, B. H. *Appl. Catal., A* **2002**, *236*, 77−89.
(60) Riedel, T.; Claeys, M.; Schulz, H.; Schaub, G.; Nam, S.-S.; Jun, K.-W.; Choi, M.-J.; Kishan, G.; Lee, K.-W. *Appl. Catal., A* **1999**, *186*, 201−213.
(61) Rasmussen, M. K.; Foster, A. S.; Hinnemann, B.; Canova, F. F.; Helveg, S.; Meinander, K.; Martin, N. M.; Knudsen, J.; Vlad, A.; Lundgren, E.; Stierle, A.; Besenbacher, F.; Lauritsen, J. V. *Phys. Rev. Lett.* **2011**, *107*, 036102.
(62) Lal, M.; Howe, A. *J. Solid State Chem.* **1981**, *39*, 368−376.

DOI: 10.1021/acscatal.7b01822
ACS Catal. 2017, 7, 7610−7622